Accounting for heterogeneity in θ - σ relationship: application to wheat phenotyping using EMI

Guillaume Blanchy*, Christopher W. Watts, Rhys W. Ashton, Colin P. Webster, Malcolm J. Hawkesford, William R. Whalley, Andrew Binley

G. Blanchy and A. Binley, Lancaster University, Lancaster, Lancashire LA1 4YW, UK; C. W. Watts, R. W. Asthton, C. P. Webster, M. J. Hawkesford and W. R. Whalley, Rothamsted Research, Harpenden, Hertfordshire AL5 2JQ, UK. * Corresponding author: g.blanchy@lancaster.ac.uk

Core ideas

- field-scale relationships between θ and electrical conductivity can be inappropriate
- pedophysical parameters can, in some cases, be approximated using baseline data
- the method is illustrated for application of EMI mapping for phenotyping wheat crops

Keywords

electromagnetic induction, agrogeophysics, hydrogeophysics, pedophysical relationship, wheat phenotyping, time-lapse

Abstract

Geophysical methods, such as electromagnetic induction (EMI), can be effective for monitoring changes in soil moisture at the field scale, particularly in agricultural applications. The electrical conductivity (σ) inferred from EMI needs to be converted to soil moisture content (θ) using an appropriate relationship. Typically, a single global relationship is applied to an entire agricultural field, however, soil heterogeneity at the field scale may limit the effectiveness of such an approach. One application area that may suffer from such an effect is crop phenotyping. Selecting crop varieties based on their root traits is important for crop breeding and maximizing yield. Hence, high throughput tools for phenotyping the root system architecture and activity at the field-scale are needed. Water uptake is a major root activity and, under appropriate conditions, can be approximated by measuring changes in soil moisture from time-lapse geophysical surveys. We examine here the effect of heterogeneity in the θ-σ relationship using a crop phenotyping study for illustration. In this study, the θ-σ relationship was found to vary substantially across a field site. To account for this, we propose a range of local (plot specific) θ-σ models. We show that the large number of parameters required for these models can be estimated from baseline σ and θ measurements. Finally, we compare the use of global (field scale) and local (plot scale) models with respect to ranking varieties based on the estimated soil moisture content change.

1 Introduction

Over the past two decades there has been a growth in the use of geophysical methods in agriculture (Allred et al., 2008). This has been driven, in part, by the need to assess variation in soil properties in a non-invasive manner over relatively large scales. Geophysical methods in such a context are a subset of proximal soil sensing approaches (Viscarra Rossel et al., 2011). Measurements of properties, such as electrical conductivity, are typically treated as a proxy for a soil property or state of interest, e.g. soil texture, bulk density or soil moisture content. Such methods may also be used in a time-lapse manner to examine changes in soil properties or states, e.g. changes in texture or soil density due to land management practices. Typically, maps of a geophysical property are presented in a qualitative manner. Whilst this can be effective in some cases, the ability to estimate quantitatively the property, or state, of interest offers greater scope for a wider range of agricultural applications. To achieve such quantification, the relationship between the geophysical proxy and the soil property or state is required. Such relationships may be spatially variable, particularly over field scales typical in agricultural studies. Here, we assess such heterogeneity in a wheat phenotyping study, and propose practical methods to account for such variability.

1.1 Field-scale phenotyping bottleneck

Wheat is one of the main staple crops in the world. It has been bred over centuries for specific traits, most of which are above-ground characteristics. Given uncertain future climatic conditions, there are demands for more resilient breeds. A key component of such resilience lies in the root system of the crop. Deeper root systems are correlated with higher yield and higher resistance to drought (Wasson et al., 2012). Usually the root system of a crop is assessed in the lab or in the greenhouse. However, field studies of the

root system are essential to understand more about how each variety adapts to its environment. The typical approach of assessing the root system of a crop in the field is by direct sampling (Wasson et al., 2014). Such methods are destructive, labour-intensive and expensive in a conventional breeding program with a large number of breeding lines. An alternative, less-invasive, and quicker approach is to consider the root activity rather than the quantity of roots. Such methods rely on observing changes in soil moisture to infer root activity (e.g. Michot et al., 2003; Srayeddin and Doussan, 2009; Garré et al., 2013; Beff et al., 2013). Different methods to measure efficiently this change in soil moisture were explored by Whalley et al. (2017) for different wheat genotypes. Among them, geophysical methods, such as electrical resistivity tomography (ERT) and electromagnetic induction (EMI) appear promising as a means of measuring a proxy to observe the dynamics of soil moisture of the subsurface (Binley et al., 2015). Shanahan et al. (2015) illustrate the use of EMI for differentiating soil drying from different wheat genotypes in a phenotyping context. In their study the relationship between the observed proxy (soil apparent electrical conductivity) and soil moisture content was assumed to be homogeneous across the study site. Huang et al. (2018) also use EMI as a proxy for plot-scale crop water of different chickpea genotypes. Other examples of the use of EMI in crop-related studies include Cassiani et al. (2012), von Hebel et al. (2014) and Moghadas et al. (2017).

1.2 Electromagnetic induction

The EMI method measures the soil apparent electrical conductivity (σ_a) in a non-contact/invasive manner. A standard EMI device is composed of a transmitter (Tx) coil and at least one receiver (Rx) coil. The transmitter coil generates a transient electromagnetic field. This primary field induces eddy currents in the ground; the magnitude of eddy currents generated is a function of the soil electrical conductivity, σ. The eddy currents

then induce a secondary electromagnetic field. Both primary and secondary electromagnetic fields are measured by the receiver coils. The out-of-phase component of their complex ratio is used to compute the apparent electrical conductivity (σ_a) of the subsurface. EMI measurements can be made in vertical and horizontal coplanar orientations, with different depth-sensitivity functions. Several current instruments, such as the one used in this study (Mini-Explorer from GF-Instruments, Czech Republic), have multiple receiver coils.

The relationship between depth-specific σ and measured σ_a, for a given coil orientation and the distance between the Tx and Rx, can be described using a simple function: the 'cumulative sensitivity function' (McNeill, 1980). A more accurate, but more complex, method based on Maxwell's equations (von Hebel et al., 2014; Andrade et al., 2016) can also be used to describe such a relationship. Using measurements made on a multi-coil device, depth-specific σ can be determined from inverse modelling of the σ-σ_a relationship. The inversion process seeks the best distribution of depth-specific σ that is consistent with all observed σ_a values for different coil spacings and orientations. A prerequisite, considered by some authors, for inversion is that the apparent values given by the different EMI configurations need to be calibrated with results from an ERT survey (e.g., Lavoué et al., 2010). More details about EMI inversion can be found in von Hebel et al. (2014).

EMI measurements have been extensively used to map field heterogeneities and produce detailed soil maps for the definition of management zones in precision agriculture (Corwin and Lesch, 2003; King et al., 2005; Brevik et al., 2006). More recently, multi-coil EMI instruments have provided greater depth-specific information in agricultural studies, allowing assessments of depth specific σ and their link to aboveground crop performance indicators (von Hebel et al., 2018; Brogi et al., 2019).

1.3 Soil moisture content – electrical conductivity relationships

The soil electrical conductivity is controlled by a number of properties (soil texture, organic matter content) and states (soil temperature, pore water electrical conductivity, bulk density, soil moisture content). The soil structural state and its properties control σ through pore connectivity and porosity. Such properties are also inherently linked to soil moisture content (e.g. determining residual moisture content), which has a major effect on soil σ. Temperature effects can be accounted for given local vertical soil temperature profiles, which we assume to not vary spatially inside the same field, although effects of daily or seasonal variation in temperature may need to be accounted for. The electrical conductivity of the pore water also contributes to the soil σ. In temperate climates, the variation of the pore water electrical conductivity should be minimal in rain-fed settings. However, this has a greater impact in irrigated conditions as the irrigated water (e.g. groundwater sourced) is likely to have a different ionic composition and temperature than the pore water in the surface layers of soil. In semi-arid environments, pore water conductivity effects may be significant due to enhanced salinity arising from high evaporative fluxes (Corwin and Lesch, 2005). Note that even in rain-fed environment, increase in pore-water electrical conductivity can occur due to fertiliser application.

Archie's law (Archie et al., 1942), developed for oil reservoir investigations, is a commonly used empirically derived model that relates the soil condition to the bulk σ. Waxman and Smits (1968) extended Archie's law by accounting for the effect of clay minerals (forming surface electrical conductivity). Several other approaches have been developed specifically for soils (e.g., Rhoades et al. 1976). Laloy et al. (2011) compared a range of

134 models for soil electrical conductivity, adopting the term “pedo-electrical” model to
135 differentiate this from classical petrophysical approaches.

136 Following Laloy et al. (2011), the relationship between σ and soil moisture content (θ) can
137 be expressed as:

138 $$\sigma = a\theta^n + b, \qquad [1]$$

139 where *a*, *b* and *n* are empirical parameters that depend on soil properties. Following Garré
140 et al. (2011), *a* is influenced by the pore water conductivity, soil texture and porosity; *b* by
141 the soil surface conductivity; *n* is controlled by the soil texture. When the exponent *n* is
142 close to 1, Eq.[1] can be approximated by a linear relationship.

143 The parameters of Eq. [1] may be obtained from laboratory measurements on field
144 samples (e.g., Shanahan et al. 2015) or directly in the field, for example using a trench and
145 soil moisture sensors (Michot et al., 2003; Garré et al., 2013; Beff et al., 2013). Both
146 methods provide information on a relatively small volume that might not be representative
147 of the entire field. Indeed, from field-scale observations, the different soil textural
148 properties also impact the θ-σ relationships, either when using σ_a (Stanley et al., 2014) or
149 with depth-specific σ (Jayawickreme et al., 2010). Eq. [1] is usually appropriate when the
150 soil moisture change is large and the soil heterogeneity is small. However, if significant soil
151 heterogeneity exists, the variation in the parameters in Eq. [1] may need to be accounted
152 for. This effect may be particularly important in phenotyping studies (the determination of
153 specific traits of crop varieties) since the differences in soil moisture change between crop
154 lines (varieties) may be smaller compared to other studies where different species are
155 used. Whether depth-specific or apparent values (like in this study) are considered,
156 estimates of small changes in soil moisture are likely to be affected by heterogeneity in the
157 θ-σ relationship (Eq. [1]).

158 Furthermore, in a phenotyping context, a better prediction of the soil moisture or change in
159 soil moisture from EMI is important as it can help to make the variety ranking similar to the
160 one obtained with direct soil moisture observations. Of course, if direct soil moisture data
161 are available, there is little value in additional geophysical proxy measurements. However,
162 in this study, the direct measurements allow us to determine what the maximum
163 achievable information on soil moisture content obtainable from EMI measurements might
164 be.

165 Thereforethis study aims to: (1) quantify the spatial heterogeneity of θ-σ relationships at
166 the field-scale; (2) determine its impact on the phenotype ranking of wheat lines; (3)
167 explore approaches to account for such effects using simplified but practical approaches.
168 The investigation utilises a dataset of σ and θ measurements collected during a winter
169 wheat field experiment.

170 2 Material and methods

171 2.1 Field layout

172 Measurements were made during the 2016-2017 growing season at the Warren Field
173 experimental farm (Woburn, UK 52°01'06.5"N 0°35'29.0"W) operated by Rothamsted
174 Research. The soil at the site is classified as a sandy clay loam (Distric Cambisol with 54%
175 sand, 20% silt and 26% clay, more details in Shanahan et al., 2015). The field was sown
176 with winter wheat at the end of 2016 and harvested in August 2017 (Bai et al., 2019). In
177 the experiment, 71 lines of wheat and one fallow treatment (all with 3 replicates) were
178 randomly distributed in 3 blocks. An aerial photograph showing the field experiment and
179 the 216 plots is shown in Figure 1. Out of the 216 plots (each 9 m by 1.8 m), 12 plots (4
180 varieties) were equipped with a 24-electrode electrical resistivity tomography (ERT) array

(0.25 m spacing) placed along the middle of each plot. ERT data were used to calibrate EMI measurements following Lavoué et al. (2010). All plots were equipped with a 1.5 m long neutron probe access tube positioned 1 m from the edge of the plot. The ratio counts from the neutron probe were converted to soil moisture content using a field calibration (+/- 0.01 cm^3/cm^3). In the field, temperature sensors recorded soil temperature at (0.1, 0.2, 0.3, 0.4, 0.6, 1 m depths). They were used to correct the electrical conductivity from the ERT and EMI using the ratio model (Ma et al., 2011) with a 2% increase per degree Celsius.

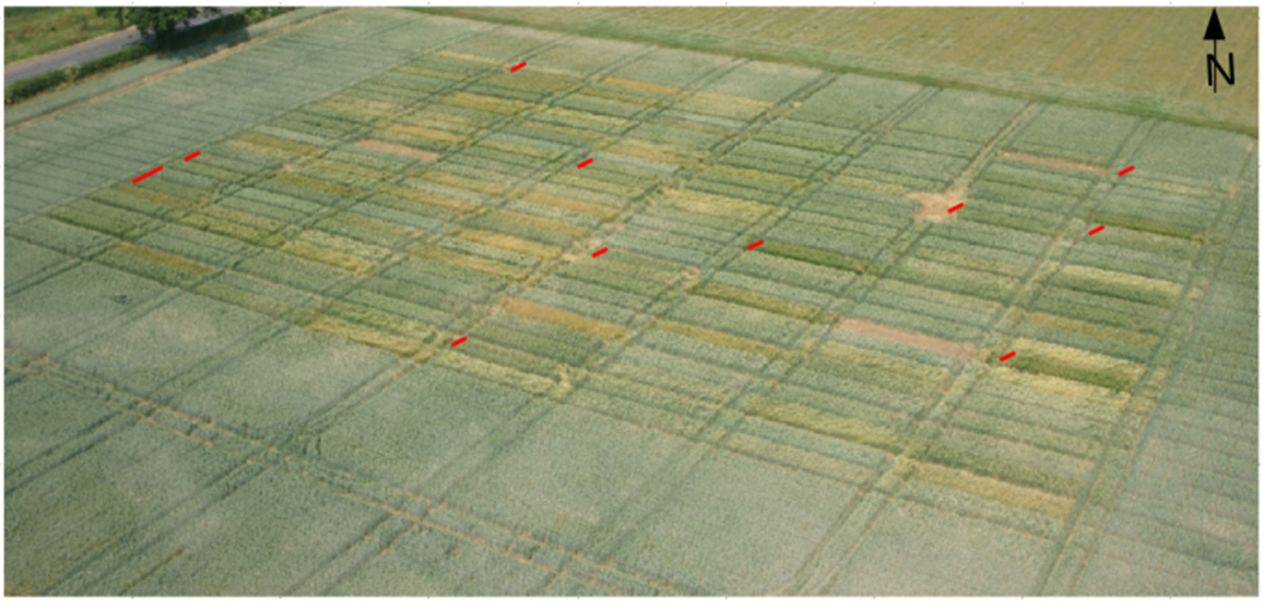

Figure 1: Aerial picture of the field showing the 216 plots (each 9 m x 1.8 m) sown with winter wheat in 2016. Plots marked in red are equipped with ERT arrays.

2.2 Field measurements

Three sets of EMI measurements were collected on each plot with a Mini-Explorer instrument (GF Instruments, Brno, Czech Republic) according to the guidelines provided in

193 Shanahan et al. (2015). They were then averaged to obtain a mean for each plot. Surveys
194 were conducted on dates (expressed in ISO 8601 format): 2016-10-08, 2017-03-02, 2017-
195 03-16, 2017-04-03, 2017-04-27, 2017-05-16 and 2017-06-01. Data from some plots were
196 discarded because of two high voltage cables buried under the field. The filtering used the
197 standard deviation of the three sets of EMI data for each plot.

198 The Mini-Explorer contains three receiver coils with separations 0.32 m, 0.71 m and 1.18
199 m from the transmitter coil. Measurements in the two modes (horizontal coplanar mode
200 (HCP) and vertical coplanar mode (VCP)) were obtained. Therefore, six measurements of
201 apparent conductivity were made. The normalised sensitivity pattern (McNeill, 1980) of
202 each configuration is shown in Figure 2a (note that in Figure 2a and hereafter the notation,
203 for example, HCP0.32, is used to identify coil orientation and spacing: HCP with a 0.32 m
204 coil spacing). Figure 2b shows example soil moisture data from the neutron probe taken at
205 seven depths. For each depth, the grey lines denote the limits used to compute the local
206 sensitivity weights used in the computation of the apparent soil moisture content (Section
207 3.1).

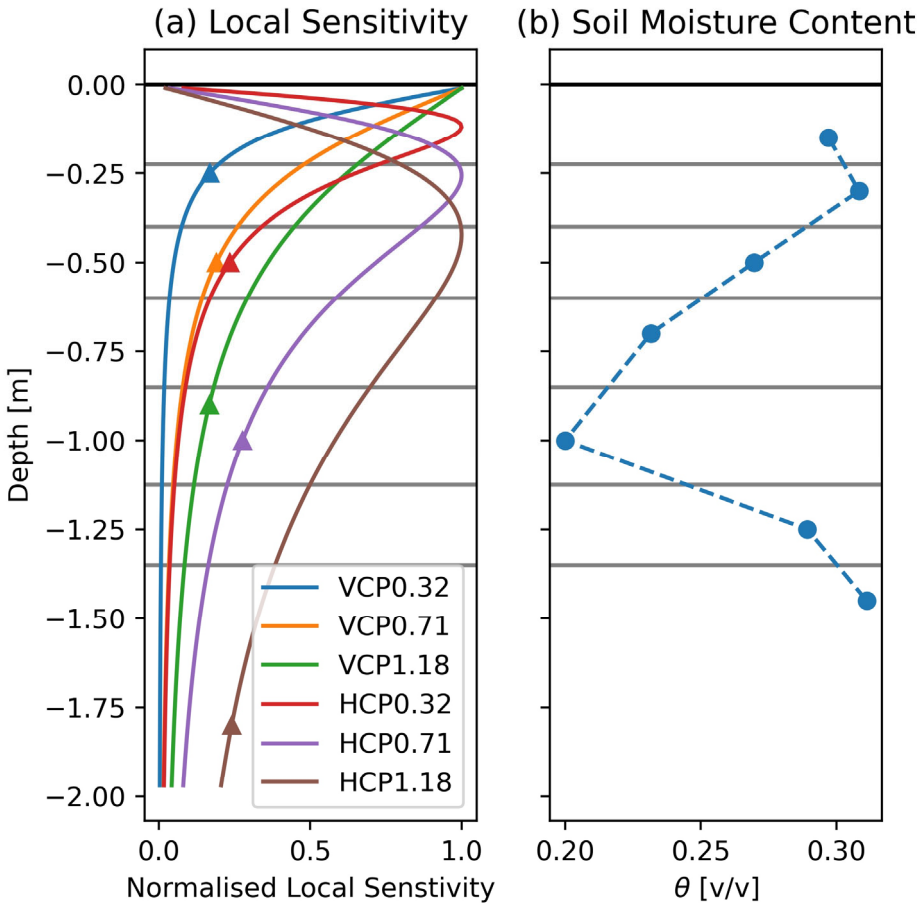

Figure 2: (a) Normalised local sensitivity pattern for the six pairs of coil orientations / coil separations available on the Mini-Explorer instrument. The triangles show the depth above which there is 70% cumulative sensitivity (commonly referred to as the effective depth of investigation). (b) shows a measured soil moisture content profile by neutron probe. To build the apparent soil moisture content, each depth-specific θ measurement is multiplied by the integrated EMI sensitivity corresponding to its depths (between the grey lines) and then summed (see Section 3.1).

208

209 ERT measurements were collected using a 48 Syscal Pro (Iris Instruments, Orléans,
210 France) on similar dates to the EMI (2017-03-02, 2017-03-16, 2017-04-03, 2017-04-27,
211 2017-05-16, 2017-06-01 and 2017-06-23). Neutron probe measurements were collected

212 on 2017-03-16, 2017-04-05, 2017-04-26, 2017-05-18, 2017-06-23. Nitrogen fertiliser
213 (Nitram 37.5% N) was applied on 2017-04-10 and 2017-04-25 as pellets. Whenever
214 possible ERT and EMI measurements were collected on the same day. Neutron probe
215 datasets were collected as close as possible to the ERT/EMI dataset, either on the same
216 day or before/after an interval of a few days, thus minimizing disturbance from any rainfall
217 events. Note that the neutron probe dataset of mid-May was taken after a large overnight
218 rainfall event. This had an impact on the shallow measurements (0.15 and 0.30 m depths)
219 but did not influence the deeper measurements. Note also that nitrogen fertiliser was
220 applied just before the measurement at the end of May. However, because of its
221 application as dry pellets and the lack of large rainfall events, it is unlikely that it had fully
222 dissolved into the soil at the time of the end of May survey. This could have caused a
223 significant increase in the pore water electrical conductivity and hence in our EMI/ERT
224 measurement, however, no sharp increase in observed electrical conductivity is apparent.
225 At the end of the field campaign, four different datasets of ERT, EMI and neutron probe
226 measurements were available to derive pedophysical relationship for each plot. Despite
227 the limited number of time-lapse data collected on the same plot, the larger number of
228 plots screened enables us to capture well the temporal and spatial variability across the
229 field.

230 # 3 Results

231 ## 3.1 Apparent soil moisture content

232 To allow comparison with observed apparent conductivity measurements and to avoid any
233 inversion artefacts that can arise from EMI inversion, an ‘apparent’ soil moisture was
234 computed based on the weights of the EMI cumulative sensitivity function (Figure 2a)
235 following the approach given by (Martini et al., 2017). The θ measurements of a given

236 profile (Figure 2b) were multiplied by their respective depth-specific normalised local
237 sensitivity and then summed to obtain an apparent soil moisture content (θ_a). The shape of
238 the normalised sensitivity function is determined by the same parameters as for the EMI:
239 the coil orientation (HCP or VCP) and the coil spacing (0.32, 0.71 or 1.18 m). Thus, for
240 each pair of coil orientation/coil spacing, a different θ_a was obtained, for comparison with
241 the observed σ_a from EMI. The apparent soil moisture content θ_a is given by

242 $$\theta_a = \Sigma_i^n \theta_i s_i, \quad [2]$$

243 where, θ_i is the measured soil moisture content of layer *i* and s_i is the sensitivity of the
244 layer *i* derived by integrating the cumulative sensitivity function between the top and the
245 bottom depths of the layer (Figure 2). Note that the sum of s_i for the profile is equal to 1. *n*
246 is the number of layers.

247 3.2 Evolution

248 Figure 3a shows the different collection times as well as selected weather data during the
249 experiment. Figures 3b, c and d show the evolution of the different observed and
250 computed below-ground variables. Note the clear difference between the averages of the
251 fallow and cropped plots, demonstrating a substantial effect of the crop in the soil moisture
252 changes over time, i.e. crop water uptake accounts for a substantial change in soil
253 moisture. Note that the σ_a from EMI shows a peak around 2017-03-01 and 2017-06-01.
254 This can be explained by the large amount of rainfall on the previous day. Note that no soil
255 moisture content data were collected on 2017-06-01, hence the series does not show a
256 similar increase. The analysis uses the data from the four following dates for which EMI,
257 ERT and neutron probe measurements were all available: 2017-03-16, 2017-04-05, 2017-
258 04-26, 2017-05-18.

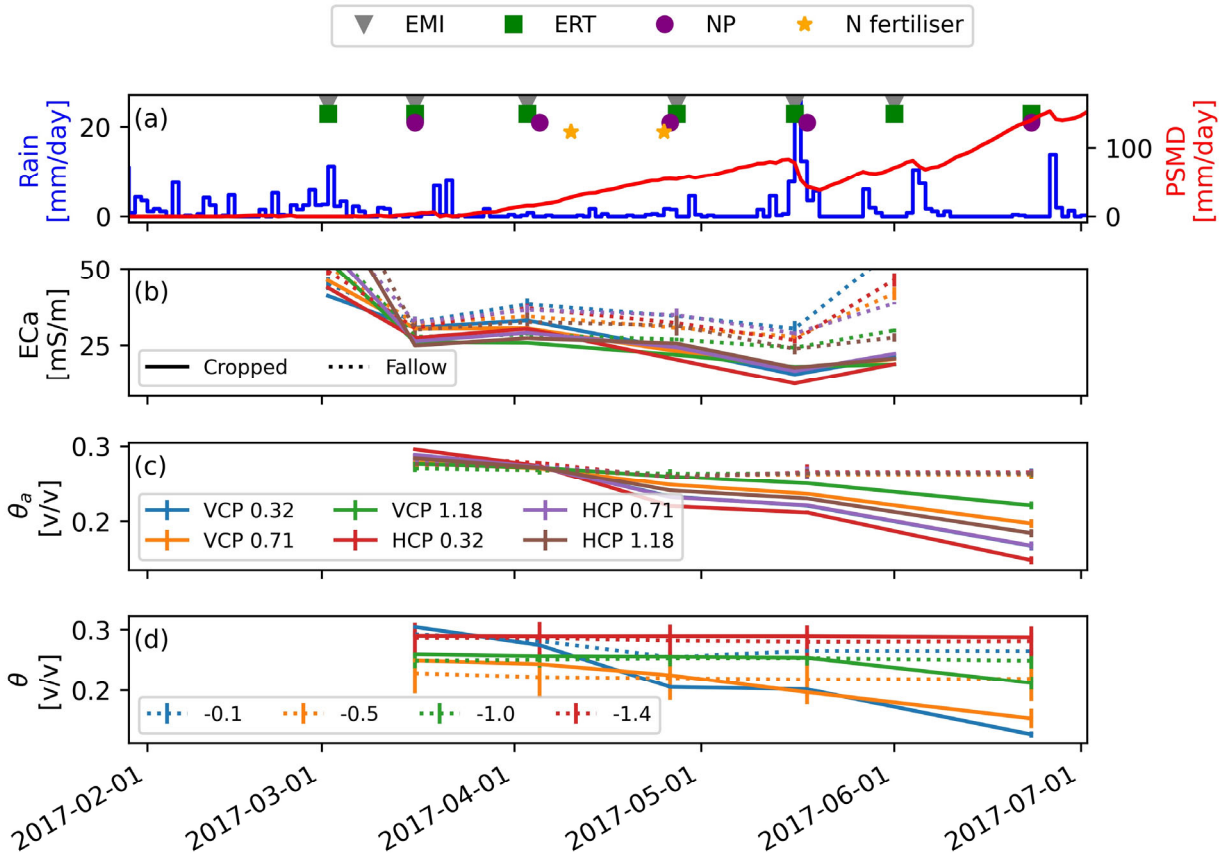

Figure 3: (a) Rainfall and potential soil moisture deficit (PSMD) with markers corresponding to the collection date of the ERT, EMI and neutron probe (NP) dataset.(b) Evolution of σ_a from EMI. (c) Evolution of computed θ_a. (d) Evolution of the measured soil moisture content from neutron probe for selected depths. Error bars are standard error of the mean (sometimes too small to be visible on the graph). Dotted lines are averages of the fallow plots while solid lines are averages of the cropped plots.

259

260 3.3 Time-lapse approach

261 Time-lapse monitoring of σ allows the removal of stationary effects of the soil (soil organic
262 matter, soil texture) on the θ-σ relationship (e.g., Robinson et al. 2012; Shanahan et al.
263 2015). This approach relies on the measurements of a baseline (in this case, where no

crop effect is present), which is usually made at the beginning of the growth season when the field is at or near field-capacity. All subsequent surveys can be compared to this baseline, consequently revealing the main drying pattern mainly driven by root activity. For the experiment presented here the baseline data was measured on 2017-03-16.

There are two ways to compute changes from the baseline conditions: (1) by computing the *difference;* (2) by computing the *relative change*. Assuming a linear relationship between θ and σ ($n=1$ in Eq. [1]) the following equations can be written.

The difference is simply the difference between σ and σ_{ref}:

$$\Delta\sigma = \sigma - \sigma_{ref} = (a\theta + b) - \left(a\theta_{ref} + b\right) = a\Delta\theta, \quad [3]$$

where σ_{ref} and θ_{ref} are the baseline σ and θ, respectively.

The relative change is the difference between σ_1 and σ_{ref} normalised by the baseline σ_{ref} (Eq. [4]). It is given by:

$$\frac{\Delta\sigma}{\sigma_{ref}} = \frac{a\Delta\theta}{a\theta_{ref}+b}. \quad [4]$$

Computing differences (Eq. [3]) removes the effect of 'offset' b but retains 'slope' a, which may vary across the site. In contrast, working with relative change (Eq. [4]) retains the effects of a and b, unless b is relatively small. In the latter case, Eq. [4] can clearly be simplified to link directly the relative change in σ with the relative change in θ as:

$$\frac{\Delta\sigma}{\sigma_{ref}} = \frac{\Delta\theta}{\theta_{ref}}. \quad [5]$$

The expressions above were used to explore ways in which the variation of a and b within a site can be accounted for.

3.4 Observations

Figure 4 shows the different relationships between σ_a and θ_a for three plots with the same variety in the field site. The variation between the three responses (expressed as absolute, difference or relative change) reveals the effect of spatial variability across the site, highlighting the limitation of adopting a single global relationship.

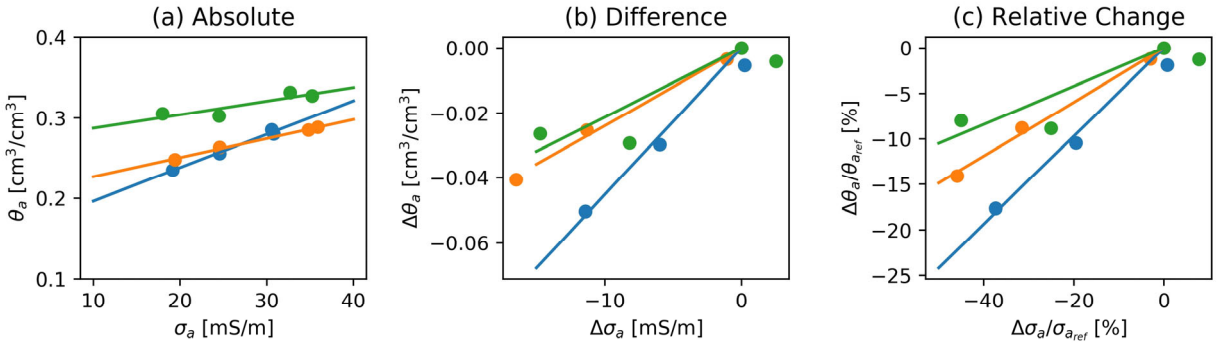

Figure 4: θ-σ relationships between θ_a and σ_a collected in the field in three example plots with the same variety expressed as: (a) absolute, (b) difference and (c) relative change. Data for each plot are differentiated by a different colour symbol/line.

Figure 4 shows the distribution of θ_a and σ_a in April 2017 and their respective difference with respect to the baseline in March 2017 (2017-03-16). From Figure 5, it can be seen that the patterns for both absolute and differences are different. This illustrates the effect of different *θ-σ* relationships observed in Figure 4. Both patterns in σ_a and θ_a values remain consistent for the different collection dates.

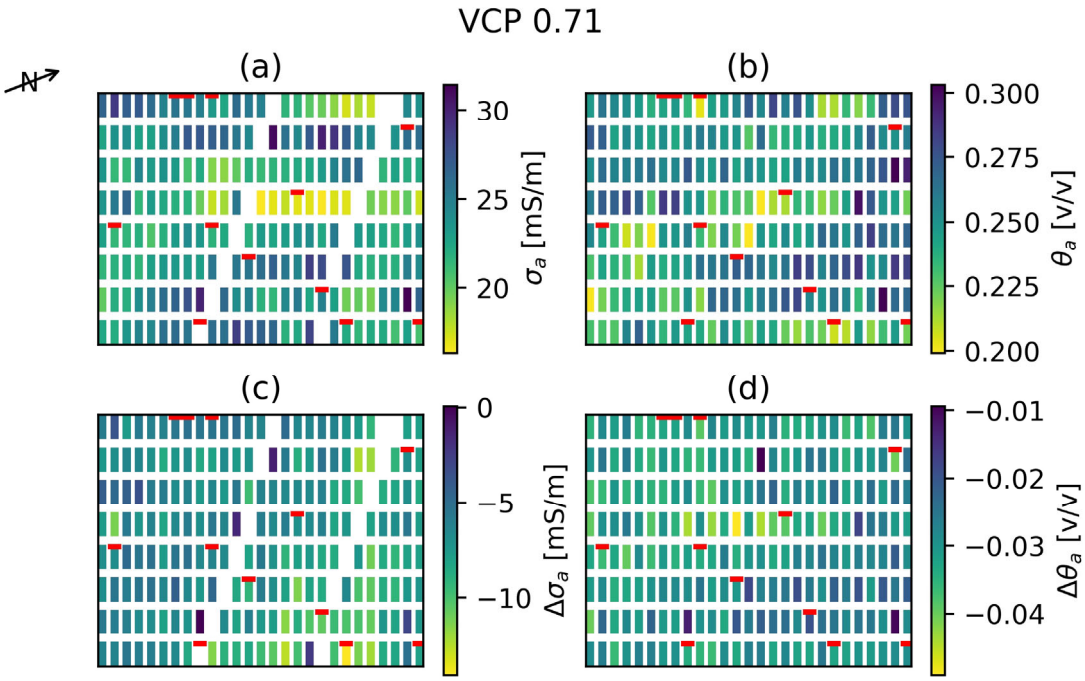

Figure 5: General schematic layout of the random block experiment (not to scale) on 2017-04-17. One rectangle represents one 9 m by 1.8 m plot. Plots marked with a red line were equipped with an ERT array. The σ_a value for each plot is the average of three replicates. (a) Shows the distribution of σ_a (VCP0.71 with an effective depth of 0.5 m). (b) Shows the corresponding θ_a from neutron probe measurements. (c) and (d) show the difference in σ_a and θ_a, respectively, from the baseline measurement of 2017-03-16. Spatial heterogeneity exists in both variables and even in their differences. Blank plots in the EMI maps are plots affected by buried high-voltage cables.

295

296 3.5 Development of local model

297 Typically, a few samples from the field are collected to build a *global* unique relationship
298 between θ and σ. We can express this relationship as:

$$\sigma = a_g\theta + b_g, \quad [6]$$

$$\Delta\sigma = a_g\Delta\theta, \quad [7]$$

where the global a_g and b_g parameters are identical for all the plots.

However, for a heterogeneous field, using this global relationship may lead to substantial errors in the estimation of soil moisture content changes. In order to overcome this, we explored *local* models allowing the assignment of a unique θ-σ relationship for each plot.

(M1) *Linear local* model: based on Eq. [1] assuming n=1. This model has two plot-specific parameters: i is the plot number, the slope is a_i and the offset is b_i

$$\sigma = a_i\theta + b_i. \quad [8]$$

Figure 6 illustrates, using all measurements, how well the linear global model and linear local model (M1) perform. There is a clear (and expected) improvement of the prediction of soil moisture content with the linear local model. Note that an exponential model (not shown here) following Eq. [1] was also fitted and has similar performance to the linear model (R^2=0.37 for the global exponential model; R^2=0.82 for the local exponential model). Consequently, the linear model is adopted hereafter.

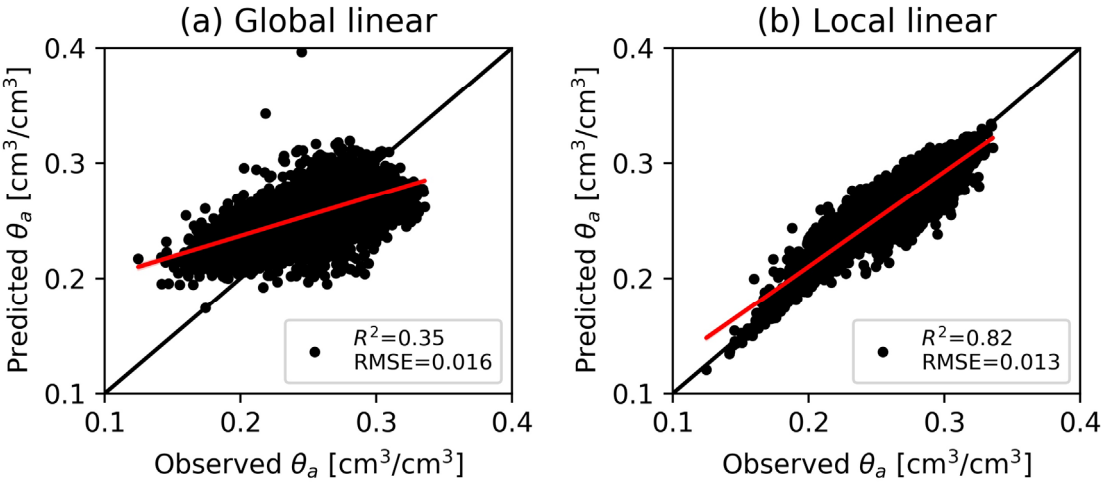

Figure 6: Both graphs show the observed θ_a vs the predicted θ_a from (a) the global linear model (Eq. [6]) and (b) the local linear model (Eq. [8]).

As seen in Figure 6, the local linear model outperforms the global linear model but increases the number of parameters needed. More importantly, a full set of monitored soil moisture content values is needed, making the geophysical proxy approach redundant. As a first step to reduce the number of local parameters, we introduce two new models.

(M2) M*ulti-offsets* model: a linear model where each plot has its own offset b_i but share a common slope a_g,

$$\sigma = a_g\theta + b_i. \quad [9]$$

(M3) *Multi-slopes* model: this model only applies to differences in values and is based on Eq. [3], each plot having its own slope a_i. This model has one parameter per plot (slope),

$$\Delta\sigma = a_i\Delta\theta. \quad [10]$$

Mathematically, the multi-offsets model (M2) produces a set of parallel σ-θ relationships similar to Figure 4a while the multi-slopes model leads to a set of conical $\Delta\sigma$-$\Delta\theta$ relationships similar to Figure 4b. Both use fewer parameters than the local linear model (M1). The rationale for these simpler models is the need to reduce the number of parameters needed and increase our ability to predict them using a set of baseline measurements.

3.6 Development of predicted local (plocal) models

All local models (M1 to M3) require large amount of information for each plot and have limited practical use in a field phenotyping application. As stated above, if direct

measurements of soil water were available in a field experiment there would be no benefit or value in using alternative geophysical proxy measurements. However, they allow us to determine what the maximum achievable information on soil moisture content obtainable from EMI measurements might be. As a more practical solution we explore a range of alternative approaches where the local θ-σ relationship is known for a subset of plots and the geophysical data are used to predict those local relationships for the other plots (*plocal*).

3.6.1 Predictors of the local parameters

The first step in developing predicted local (plocal) models is to identify the best estimates of the local parameters among baseline measurements. Figure 7 shows the relationship between the different local parameters from each model (M1 to M3) and the baseline σ_a and θ_a. It can be observed for the linear local model (M1) that the local offsets (b_i) are well related to baseline θ_a^{ref} and that the slopes (a_i) are more related to σ_a^{ref}. The multi-offsets (M2) and multi-slopes (M3) models aim to amplify those trends by reducing the number of local parameters. Using multiple local offsets but a global slope (Eq. [9]), the multi-offsets model (M2) displays a stronger relationship with the baseline θ_a^{ref} (R^2=0.86) than the linear model (R^2=0.40). Using multiple local slopes and no offsets (Eq. [10]), the multi-slopes model (M3) displays a stronger relationship with the baseline σ_a^{ref} (R^2=0.33) than the linear model (R^2=0.27).

VCP 0.71

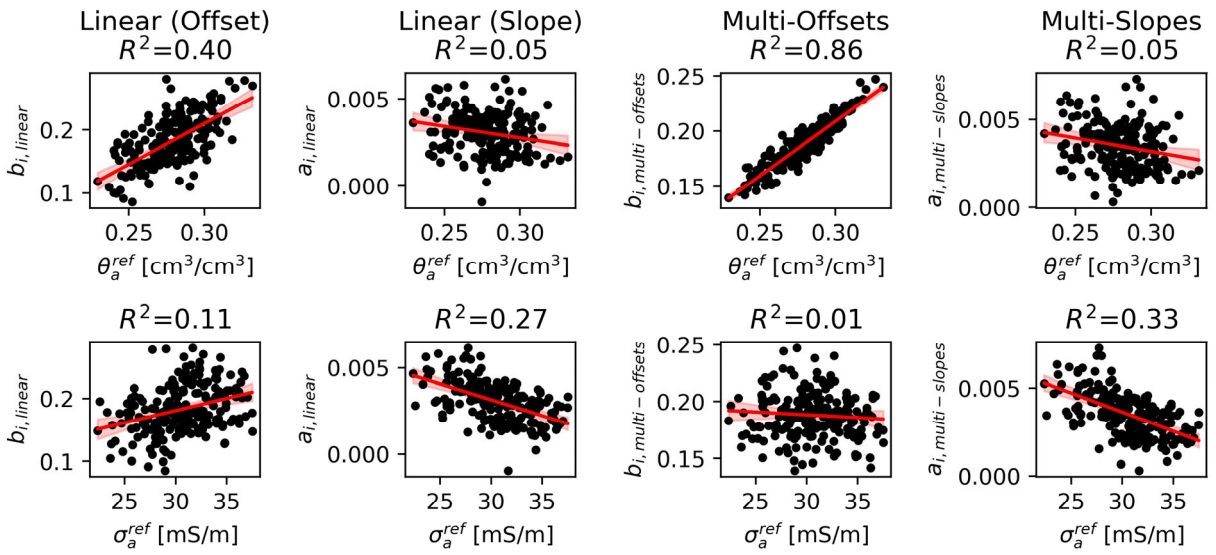

Figure 7: Relationships between the local parameters of the three local models (M1 to M3) and the two baseline measurements σ_a^{ref} and θ_a^{ref} for VCP0.71. The first two columns on the left shows the local offsets b_i and the local slopes a_i of the local linear model (M1) against the baseline measurements. The 3rd column shows the local offsets b_i of multi-offsets model and the 4th column shows the local slopes a_i of the multi-slopes model against the baseline measurements. The red line is the line of best fit with its 95% confidence interval (red shaded region).

353

354 Figure 7 allows the identification of the best predictor for each local parameter. Given local
355 parameters from a subset of plots, a linear relationship between them and their best
356 predictor is derived and used to predict the value of the local parameters for the other
357 plots. Those predicted local parameters are then used in one of the models (M1 to M3).
358 This process and the results are shown below for the multi-offsets (M2) and the multi-
359 slopes (M3) models (M1 not shown). Hereafter, the subset of plots is composed of the 12
360 plots equipped with an ERT array as they are randomly distributed in the field. The choice

of plots is somewhat arbitrary: another set of plots could have been selected but they should span the largest possible range of σ and θ observed in the field.

3.6.2 Multi-offsets model

The multi-offsets (M2) model incorporates a local offset, b_i, but a global slope, a_g (Eq. [9]). As an illustration, Figure 8a compares, for a subset of plots (black line and dots), the multi-offsets model with its corresponding global model for VCP0.71. The global model compared here corresponds to Eq. [6] where both slope, a_g and offset b_g are uniform across the field. The multi-offsets model improves the accuracy of the predicted θ_a compared to the global model (R^2=0.92 vs 0.37) due to the inclusion of the local parameters b_i (Figure 8a). Both models are fitted on all the plots available. In order to decrease the amount of data needed to obtain these local offsets, a linear relationship between the local offsets b_i and the baseline θ_a^{ref} is derived using the data from a subset of plots (Figure 8b). This b_i – θ_a^{ref} relationship is then used to predict b_i for all the plots. Finally, in Figure 8c, those predicted offsets are used in the plocal multi-offsets model to obtain θ_a. In this case, the R^2 of the multi-offsets model with the predicted parameters (0.81) is better than for the global fit (0.37).

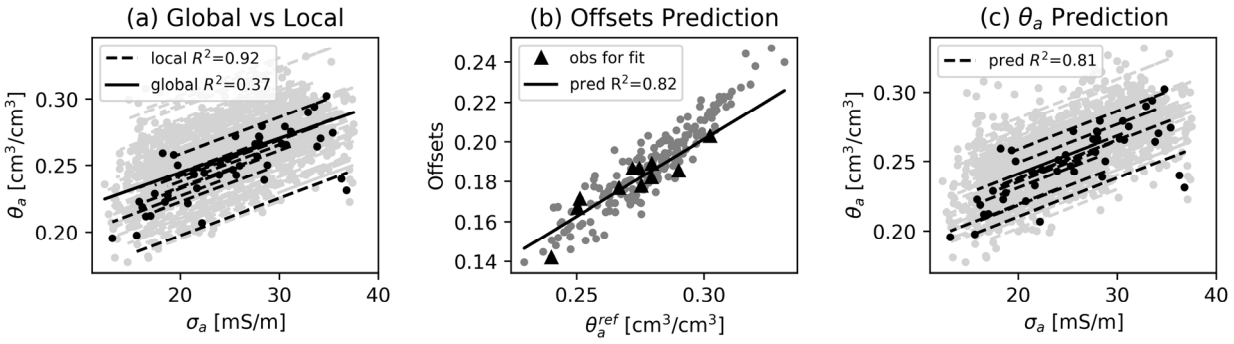

Figure 8: Multi-offsets model fitted with apparent values (VCP0.71). The grey dots show all the data available on the 216 plots. They represent the maximum number of

information achievable if both σ and θ are monitored on all the plots. In a more practical situation, only a subset of plots (black dots) are monitored for both σ and θ. (a) Shows the relationship fitted with the multi-offsets model (local) as well as a global linear model, both fitted on the 216 plots. (b) Shows the local offsets b_i vs the baseline θ_a^{ref}. The black line corresponds to a linear relationship fitted on the subset of plots. This relationship is used to predict the offsets for all the other plots. (c) Shows the multi-offsets model using the predicted offsets (plocal) from (b). In subplots (a) and (b) the black dots and dashed lines are used to illustrate the behaviour of some plots as plotting all lines will make the graph unreadable.

377

378 The multi-offsets model focuses on the absolute values and not the differences. For the
379 latter the multi-slopes model is adapted further.

380 3.6.3 Multi-slopes model

381 The multi-slopes model (M3) presented in Figure 9 tries to fit a local model $\Delta\sigma_a$ and $\Delta\theta_a$
382 (Eq. [10]). Figure 9a shows a comparison of the multi-slopes model and its global
383 equivalent. In this case the global model contains a unique slope for the whole field.
384 Similar to Figure 8, the introduction of a local parameter (slope a_i) improves the strength of
385 the relationship from R^2 0.71 to 0.86. In Figure 9b, a linear relationship is derived between
386 the local slopes a_i and the baseline σ_a^{ref} based on a subset of plots (R^2 0.64). This a_i-σ_a^{ref}
387 relationship is then used to predict the values of a_i for all the other plots. Finally, those
388 predicted slopes are used in Figure 9c in the multi-slopes model to predict $\Delta\theta_a$ for all plots.
389 The multi-slopes model with the predicted local parameters (plocal) has a higher R^2 (0.68)
390 than the global fit (0.71).

391

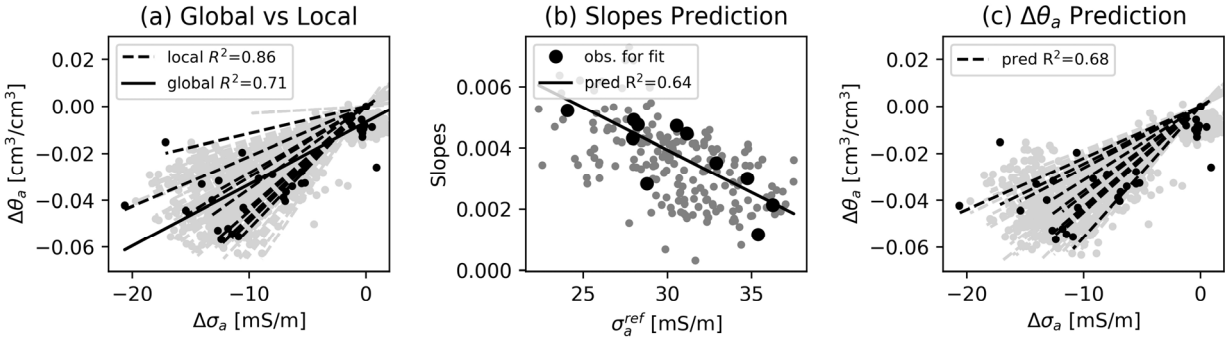

Figure 9: Multi-slopes model fitted with differences in apparent values (VCP0.71). The grey dots show all the data available on the 216 plots. They represent the maximum number of information achievable if both σ and θ are monitored on all the plots. In a more practical situation, only a subset of plots (black dots) are monitored for both σ and θ. (a) Shows the multi-slopes model as well as a global relationship with a unique slope for all 216 plots (global). (b) Shows the local slopes according to the baseline σ_a^{ref}. The black line corresponds to a linear relationship fitted on a subset of plots. This relationship is used to predict the local slopes for all the other plots. (c) Shows the multi-slopes model using the predicted slopes from (b) (plocal). In subplots (a) and (b) the black dots and dashed lines are used to illustrate the behaviour of some plots as plotting all lines will make the graph unreadable.

392

393 3.7 Quality of the predicted local models

394 *Figure 10* shows the quality of the prediction of M1, M2 and M3 using the predicted local
395 parameters (*plocal*). The multi-offsets (M2) and multi-slopes (M3) models which only have
396 one local parameter show better R^2 (M1: 0.16, M2: 0.53, M3:0.60) and a lower root mean
397 squared error (RMSE) (M1: 0.04, M2: 0.02, M3:0.02) than the plocal linear model (M1)
398 which has two local parameters. That means that the predicted soil moisture content from

the multi-offsets (M2) or multi-slopes (M3) models is more accurate than from the linear model (M1).

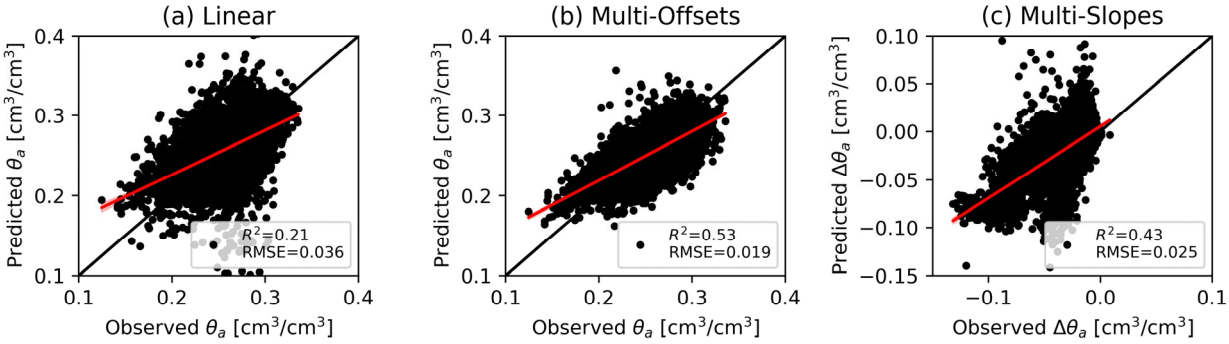

Figure 10: Quality of the predicted θ_a vs the observed θ_a from (a) linear, (b) multi-offsets and (c) multi-slopes models with predicted local parameters. The red line is the line of best fit with its 95% confidence interval (red shaded region). Both multi-offsets and multi-slopes models have one local parameter while the linear model has two.

3.8 Choice of the size of the subset of plots for plocal models

The size of the subset of plots needed for the plocal models needs to be chosen carefully. Figure 11 shows the effect of the number of selected plots on the RMSE of the prediction for the multi-offsets (M2) and the multi-slopes (M3) models. In this case, the RMSE does not change much if more than 10 plots are included in the subset.

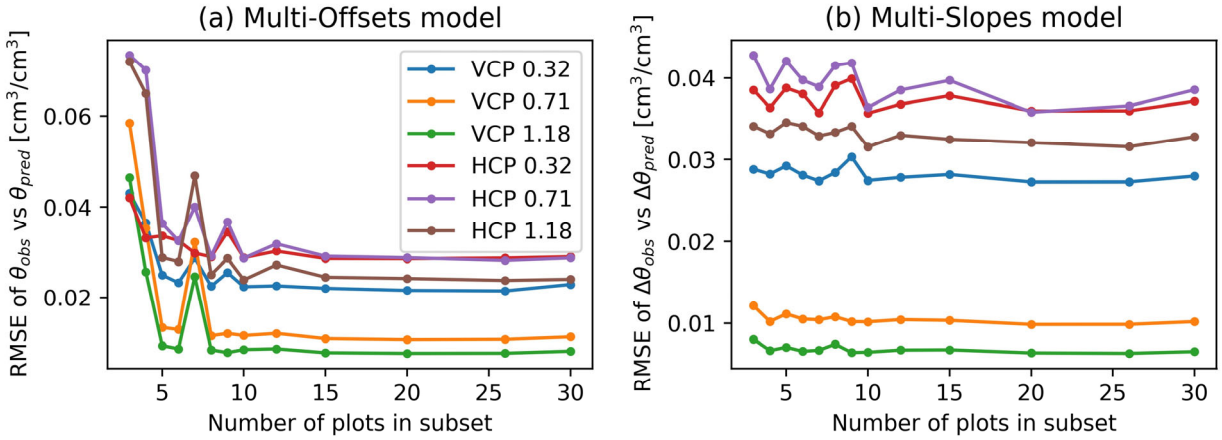

Figure 11: Effect of the size of the subset of plots on the predictions of the plocal multi-offsets (a) and multi-slopes (b). After sorting the plots according to the baseline σ_a, a subset of a given number of plots is selected at regular interval on the whole range of baseline values.

407

408 3.9 Effect on the variety ranking

409 In a phenotyping context, we expect similarity in the rank of varieties whether observed
410 (from neutron probe) or predicted (from EMI) soil moisture values are used. To assess the
411 ranking improvement the predicted values of the global, local and plocal models are
412 averaged by variety. Then the Spearman's rank correlation is computed between the
413 observed and the predicted θ_a (or $\Delta\theta_a$). The Spearman's rank correlation has the
414 advantage to be directly related to the ranking of the variety which is a commonly used
415 metric in crop breeding. A high value for this coefficient means, in our case, that higher
416 predicted θ_a is associated with higher observed θ_a or that larger predicted θ_a differences
417 are associated with larger observed θ_a differences, from examining absolute values or
418 differences, respectively.

Figure 12a shows the Spearman's rank correlations for the multi-offsets (M2) model using the baseline θ_a^{ref} as predictor of the local offsets. Figure 12b shows the Spearman's rank correlations for the multi-slopes (M3) model using the baseline σ_a^{ref} as predictor of the local slopes.

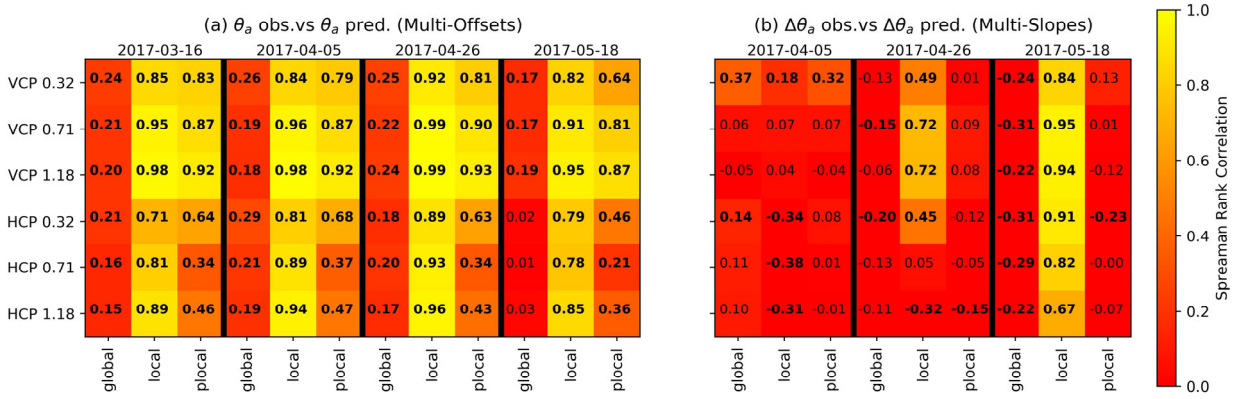

Figure 12: Improvement in variety ranking in terms of the Spearman's rank correlation coefficient for (a) the multi-offsets and (b) the multi-slopes models. Each row of the table corresponds to a coil configuration. The columns are grouped by dates and subdivided into global, local and plocal models. The global models use field-specific parameters, the local models use plot-specific parameters estimated using all the data available. The plocal model use the predicted plot-specific parameters estimated from baseline measurements (as in *Figure 8*b and *Figure 9*b). Bold numbers denote a significant correlation ($p<0.05$).

Using the data in this study, the global models offer poor correlation compared to the local models, due to the heterogeneity of the σ-θ relationship. This is true for all coil configurations. The plocal models, i.e. the models using the predicted local parameters, show higher correlation compared to their global equivalent. For the multi-offsets model the improvement between global and the plocal is substantial (Figure 12a). When

considering changes in soil moisture content (Figure 12b), the correlation with the global model is sometimes negative. This is a concern as it means that an increase in σ_a can be associated with a decrease in θ_a following application of the global model. The local multi-slopes models increases this correlation substantially, especially for later dates. However, the plocal multi-slopes model shows relatively poor correlation even if it can compensate for the negative correlation observed in the global model in some cases.

4 Discussion

4.1 Methodological limitations

The approach presented in this manuscript relies on apparent and not depth-specific electrical conductivity measurements to avoid the uncertainty arising from EMI inversion. Hence, we converted soil moisture content to apparent values using the practical cumulative sensitivity function (McNeill, 1980). However, the latter can have limitations especially on heterogeneous conductive soils. To estimate the errors that can arise from using the cumulative sensitivity function, Maxwell's equations can be used to reconstruct sensitivity functions based on a synthetic two layers profile comparable to what is observed in the field (Callegary et al., 2007). Both sensitivity functions are then used to compute the apparent soil moisture content. The maximum discrepancy between the two approaches is 0.01 cm^3/cm^3, which is similar to the neutron probe accuracy (0.01 cm^3/cm^3). Given the magnitude of the errors, this probably has a more important impact on the changes in soil moisture content than on the absolute values. This might explain why the multi-slopes model works less well than the multi-offsets model in this study.

The dynamics of the soil moisture is complex and isolating the effect of root activity is challenging. Whenever possible, measurements were collected at increasing potential soil

452 moisture deficit and away from significant rainfall events (Figure 3). The drying observed in
453 cropped plots compared to fallow plots suggests a substantial effect of the root activity
454 (Figure 3). However, the proposed approach does not aim at univocally measuring root
455 water uptake but rather at comparing soil moisture variation mainly induced by root activity
456 for the different varieties.

457 The models described in the manuscript are simple linear models. More complex
458 relationships can be used to relate soil moisture to electrical conductivity. For example, an
459 exponential model was initially tested and showed similar performance to the linear model
460 (see section 3.5), hence the simplest model is chosen. In the linear models presented, the
461 slope can be related to the soil surface conductivity while the offset is more a function of
462 the pore water conductivity. Both are functions of the soil texture and porosity (Garré et al.,
463 2011). We do not have the information to investigate further the impact of these soil
464 properties on the pedophysical parameters we derived for this field.

465 This study assumes that the samples taken on each plot (EMI, NP) are representative of
466 the entire plot and that no substantial heterogeneity exists within the plot itself. While we
467 have no data to assess that this assumption is fulfilled for all the plots, the inverted ERT
468 sections, which span 5.75 out of the 9 meters of the plot length, suggest that this is the
469 case.

470 One can question if the plot is the appropriate scale at which to investigate the variability of
471 the θ-σ relationships. The use of variogram analysis can certainly help to determine the
472 appropriate length-scale at which the heterogeneity occurs. However, this method was not
473 explored in this study as our approach relies on the plot-scale for practical reasons and to
474 be consistent with additional phenotyping measurements at the site.

Finally, it has been assumed that the root system of the crop itself did not significantly contribute to the soil bulk apparent conductivity. While there is evidence that suggests that coarser roots can effect the soil bulk electrical conductivity (Amato et al., 2008; Mary et al., 2017), finer herbaceous roots have been found to have a signal in magnitude similar to the effect of grain size or soil moisture content (Amato et al., 2009). Nevertheless, recent studies were able to isolate the electrical signature of roots themselves (Tsukanov and Schwartz, 2020). This could have great potential for phenotyping applications.

4.2 Ranking performance

Fitting a global model with field-specific parameters to all the data can lead to a satisfactory prediction of the soil moisture content particularly if the differences expected between the treatments are large such as for different types of vegetation (Jayawickreme et al., 2010), between fallow and cropped plots or between different soil types. However, when comparing a large number of similar varieties this global model may be limited (Figure 12). In a phenotyping application, as here, using of such a relationship may lead to false ranking of variates when using geophysical data (Figure 12). As observed by Farahani et al. (2005) for non-saline soil, higher σ_a is not always associated with higher soil moisture. Taking into account differences, it can also be seen that a large reduction in σ_a is also not always associated with a large reduction in θ_a. The negative correlations sometimes observed are of concern as they lead to very different varieties ranking whether we consider σ_a or θ_a (Figure 12). The use of local parameters in the σ-θ relationship increases the Spearman's rank correlation for later dates as the soil moisture differences from the baseline become larger. The large number of parameters needed to fit the local models (linear, multi-offsets or multi-slopes) can be reasonably reduced using a relationship between the local parameters and the baseline σ_a or θ_a fitted on a subset of

plots. The resulting plocal models that use those predicted parameters increase the accuracy of the prediction compared to global models (*Figure 10*). The coefficient of determination (R^2) is often similar or higher to the ones of the corresponding global models but the ranking assessed (using the Spearman's rank correlation) is usually better (Figure 12). Note that the R^2 achieved are all below 0.6 which is relatively poor compared to what could potentially be achieved with a local relationship for all the plots (Figure 7b). Indeed, this improvement is mainly limited by the quality of the relationship between the local parameters and the predictors (Figure 8b and Figure 9b). Hence, the need to select plots which span a wide range of conductivities to be monitored for both σ and θ (see 4.4) in order to have a more robust fit that is representative of the entire field.

4.3 Local models and parameters predictability

As seen in Figure 7, the offsets of the linear or multi-offsets models are mainly related to the baseline θ_a. There is also a slight positive trend between the baseline σ_a and the offsets of the linear model but it is relatively weak compared to θ_a and it completely vanishes in the multi-offsets model. The simplification of the linear model to a multi-offsets model amplifies this dependence on the baseline θ_a. Wetter plots tend to stay wetter compared to other plots surveyed at the same time. This can be seen on Figure 4a where each plot follows its own increasing line. This strong offset effect also explains why the relative change approach described earlier does not work well in this case. Given Eq. [3], the offset is not negligible and so the equation cannot be simplified to Eq. [4]. That is why differences (Figure 4b) and relative changes (Figure 4c) are similar. If the offsets were negligible, Figure 4c would show a single line.

The local slopes of the local linear model are well correlated with the baseline σ_a. Considering differences, the multi-slopes model also shows good correlation between the

523 local slopes and the baseline σ_a. The conical shape of the data shown in Figure 4b and
524 Figure 9a for the differences illustrates how different plots have different slopes. Stanley et
525 al. (2014) show how the slopes of the σ-θ relationships vary between two sites with
526 contrasting textures: sites with higher clay content, for example, result in greater values
527 than those from sandier locations.

528 The multi-offsets and multi-slopes models have one contrasting assumption. The former
529 assumes a unique slope for the entire field while the latter uses plot-specific slopes.
530 Having both plot-specific offsets and slopes leads to the local linear model but its local
531 parameters are difficult to predict using baseline measurement (Figure 7) and hence leads
532 to poor estimates (*Figure 10*). As the relationship between σ_a-θ_a is largely offset
533 dominated, we decided to fix the slope in the multi-offsets model to reduce the number of
534 local parameters. For the differences, the effect of the offsets disappeared (Eq. [3]) and
535 only the effect of the slopes has an impact on the relationship. This leads to the multi-
536 slopes model (Eq. [10]).

537 As seen in Figure 13, the differences in observed σ_a are well correlated with the baseline
538 readings. Larger reductions in σ_a are seen on plots with higher baseline σ_a (Figure 13a).
539 Note that such a trend is not observed for θ_a (Figure 13b). The fact that the σ_a differences
540 are still function of the baseline reveals that the baseline σ_a contains some information on
541 how the σ_a is likely to change: larger reductions are expected in areas of higher baseline
542 σ_a. This behaviour explains why the starting σ_a could be a good predictor of the slopes in
543 the multi-slopes and linear models. Indeed, as the plots with higher baseline σ_a show a
544 larger increase in σ_a with time for the same increase in θ_a, they need to have a smaller
545 slope to compensate. Smaller slopes are then found for higher baseline σ_a (Figure 9b and
546 Figure 7). We believe this is related to the heterogeneity of the soil texture of the field
547 where some areas are richer in clay than others.

548

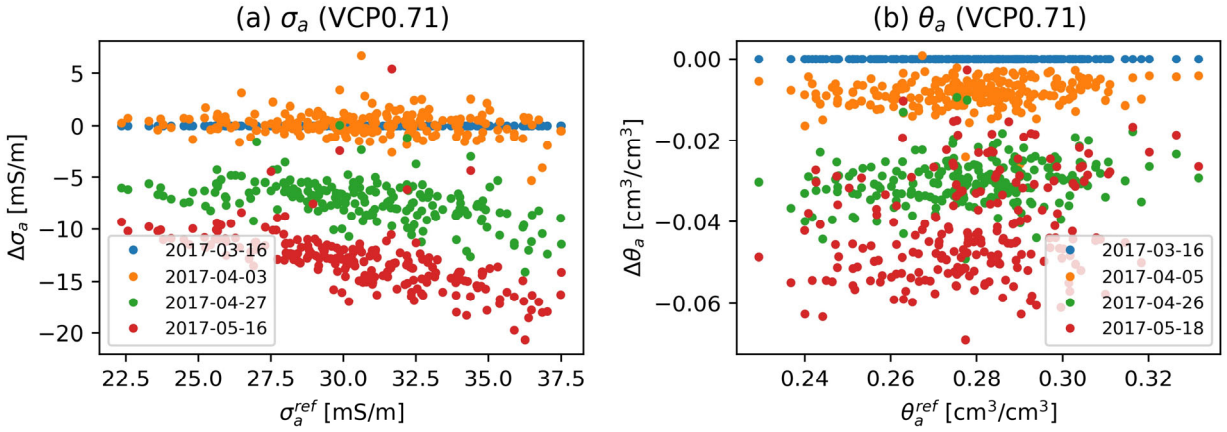

Figure 13: Differences in σ_a (a) and θ_a (b) for VCP0.71 plotted against their respective baseline measurements for the different survey dates (different colours). There is larger decrease in σ_a for higher σ_a^{ref} in (a) while such a downward trend cannot be seen for θ (b).

549

550 Plots with higher baseline σ_a tend also to have smaller offsets as well (Figure 7). But this
551 relationship is not strong enough to be used for parameter prediction and θ_a is preferred as
552 the predictor (Figure 8b). Also, the prediction of the local parameters using the baseline
553 readings is much better in the multi-offsets model (Figure 8b R^2=0.82) than in the multi-
554 slope model (Figure 9b R^2=0.64). This can explain why the multi-slopes model using
555 predicted local parameters show only a slight improvement in variety ranking compared to
556 the multi-offsets model (Figure 12).

557 The multi-offsets and multi-slopes models are simplified ways to account for the variability
558 due to the spatial heterogeneity of the θ-σ relationship. By reducing the number of local
559 parameters compared to a local linear model, the local parameters are more correlated
560 with baseline measurements and hence easier to predict based on a subset of plots. In

561 that way, they increase the ranking of the varieties and the accuracy of the predicted θ_a
562 compared to global models.

563 4.4 Improvement of the time-lapse approach

564 A key bottleneck in using the local models (M1 to M3) is the predictability of the large
565 number of local parameters they require. In this study an approach was chosen where
566 both variables (θ_a and σ_a) are recorded on a subset of plots. In this case the same 12 plots
567 that served for the ERT calibration of the EMI data were arbitrarily chosen as they are well
568 distributed across the field and span the whole range of observed baseline values. In our
569 case, a sample of 12 was a large enough number to reach the minimum RMSE achievable
570 (Figure 11). Given the local parameters found on the selected plots, a relationship can be
571 derived using the baseline σ_a or θ_a. This relationship can then be used to predict the
572 values of the local parameters for the other plots. We believe that geostatistical tools can
573 also be used to determine the number of sampling locations. However, we have not tested
574 these in this paper.

575 Considering the above, we propose an improvement to the time-lapse approach described
576 earlier to monitor the changes in soil moisture for large crop breeding experiment. After the
577 first baseline EMI survey, plots with contrasting σ_a are selected and equipped with soil
578 moisture sensors (such as neutron probe access tube). The data collected on those plots
579 will allow the estimation of the parameters for the multi-offsets and multi-slopes models.
580 Those parameters can then be expanded to the other plots using the baseline
581 measurements (Figure 8b and Figure 9b).

582 The new approach is as follows.

583 1. Baseline survey on all the plots to acquire σ_a^{ref} and θ_a^{ref}:

- multi-slopes: EMI with all configurations (σ_a^{ref});

- multi-offsets: soil moisture measurements for all depths available to build an apparent soil moisture content measurements (θ_a^{ref})

2. Selection of plots with contrasting σ_a to be equipped with θ sensors

3. Time-lapse EMI on all the plots and time-lapse θ on the selected plots: collection of multiple σ_a-θ_a datasets

4. Fit the multi-slopes (Eq. [10]) and multi-offsets (Eq. [9]) models on the selected plots to obtain the value of the local parameters: slope a_i for multi-slopes and offset b_i for multi-offset

5. Fit of linear relationship between those local parameters and the baseline value of the selected plots as in Figure 8b and Figure 9b: $a_i \sim \sigma_a^{ref}$ and $b_i \sim \theta_a^{ref}$

6. Those linear relationships are then used to predict the local parameters a_i and b_i on the other plots using their respective baseline measurements σ_a^{ref} / θ_a^{ref}

This new approach offers a trade-off between equipping all the plots with soil moisture sensors in order to fit a local models and using a unique global relationship for the entire field. Note that if a multi-offsets model is to be derived, baseline θ data are still needed as they are the best predictors of the local offsets.

4.5 Analysis of the residuals

An increase in residuals can arise due the large number of local parameters. However, as Figure 14 shows, there is no substantial increase in the distribution of those residuals for the predicted local models compared to the global and local models. We can also see from Figure 8b and Figure 9b that even if the relationship is not perfectly fitted, the predicted parameters tend to stay in a reasonable range, avoiding the generation of outliers. Note

607 that the residual for the multi-slopes model are smaller than the residuals for the multi-
608 offsets as the range of $\Delta\theta_a$ (0 to -0.07) is smaller than the range of θ_a (0.15 to 0.35).

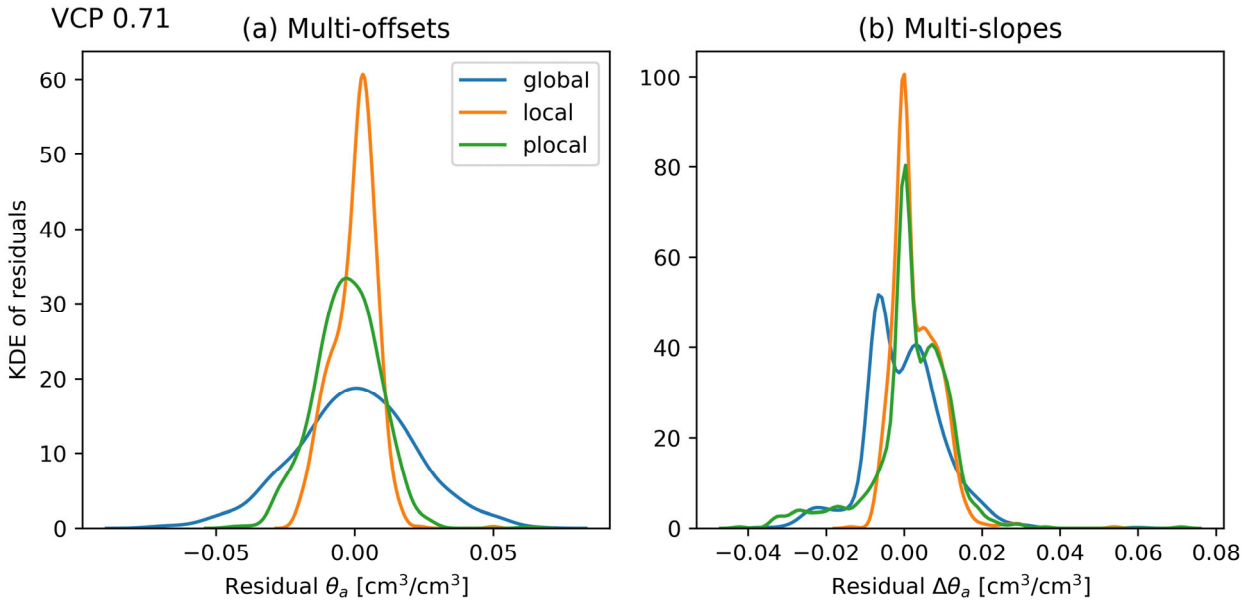

Figure 14: Kernel density estimate (KDE) of the residuals for the multi-offsets (a) and the multi-slopes (b) models for VCP0.71. For each the global model represent a global (field-scale) linear relationship while the local models use plot-specific parameters. The plocal model is the local model with the plot-specific parameters predicted from baseline θ_a or σ_a.

609

610 5 Conclusions

611 High-throughput geophysical tools, in this case time-lapse EMI, offer great potential as a
612 proxy measurement of soil moisture differences. When measurements are collected over
613 increasing soil drying during crop growth, they may be linked to root activity in non-
614 irrigated crop breeding field trials. The usual time-lapse approach is useful for removing
615 the static effects of soil electrical conductivity but can be limited for ranking a large number

of similar varieties in a heterogeneous environment. The spatial heterogeneity of the σ-θ relationship at the field scale has an impact on the ranking of the varieties and using a field-specific global relationship can lead to misleading interpretation. The proposed multi-offsets and multi-slopes models try to account for this heterogeneity by using plot-specific parameters that can be estimated from the baseline measurements. This improves the variety ranking between EMI and neutron probe data. A practical approach is proposed for such studies in which a baseline EMI survey is used to target sites for soil moisture monitoring, thus enhancing the ability to formulate predictions of the local σ-θ relationships. Although all the processing presented here was done with apparent conductivity measurements, however, the same process can be applied to depth-specific (inverted) measurements.

6 Acknowledgements

G.B. is supported by a Lancaster University - Rothamsted Research- CEH Graduate School for Environment PhD studentship. The field experiment described in the paper was funded by Syngenta Ltd. while the additional geophysical measurements were funded by the Lancaster University - Rothamsted Research- CEH Graduate School. M.J.H and W.R.W. at Rothamsted Research are supported by the Designing Future Wheat Programme by the UK Biotechnology and Biological Sciences Research Council[BB/P016855/1]. We are grateful to associate editor Ute Wollschläger, reviewer Sarah Garré and an anonymous reviewer for their comments on an earlier version of the manuscript.

7 References

Allred, B.J., J.J. Daniels, and M.R. Ehsani, editors. 2008. Handbook of agricultural geophysics. CRC Press, Boca Raton.

Andrade, F.C.M., T. Fischer, and J. Valenta. 2016. Study of errors in conductivity meters using the low induction number approximation and how to overcome them. Near Surface Geoscience 2016-22nd European Meeting of Environmental and Engineering Geophysics. EAGE, Barcelona, Spain

Archie, G.E., and others. 1942. The electrical resistivity log as an aid in determining some reservoir characteristics. Trans. AIME 146(01): 54–62.

Bai, C., Y. Ge, R.W. Ashton, J. Evans, A. Milne, et al. 2019. The relationships between seedling root screens, root growth in the field and grain yield for wheat. Plant Soil. doi: 10.1007/s11104-019-04088-9.

Beff, L., T. Günther, B. Vandoorne, V. Couvreur, and M. Javaux. 2013. Three-dimensional monitoring of soil water content in a maize field using Electrical Resistivity Tomography. Hydrol. Earth Syst. Sci. 17(2): 595–609. doi: 10.5194/hess-17-595-2013.

Binley, A., S.S. Hubbard, J.A. Huisman, A. Revil, D.A. Robinson, et al. 2015. The emergence of hydrogeophysics for improved understanding of subsurface processes over multiple scales: The Emergence of Hydrogeophysics. Water Resour. Res. 51(6): 3837–3866. doi: 10.1002/2015WR017016.

Brevik, E.C., T.E. Fenton, and A. Lazari. 2006. Soil electrical conductivity as a function of soil water content and implications for soil mapping. Precis. Agric. 7(6): 393–404. doi: 10.1007/s11119-006-9021-x.

Brogi, C., J.A. Huisman, S. Pätzold, C. von Hebel, L. Weihermüller, et al. 2019. Large-scale soil mapping using multi-configuration EMI and supervised image classification. Geoderma 335: 133–148. doi: 10.1016/j.geoderma.2018.08.001.

Callegary, J.B., T.P.A. Ferré, and R.W. Groom. 2007. Vertical Spatial Sensitivity and Exploration Depth of Low-Induction-Number Electromagnetic-Induction Instruments. Vadose Zone J. 6(1): 158. doi: 10.2136/vzj2006.0120.

Cassiani, G., N. Ursino, R. Deiana, G. Vignoli, J. Boaga, et al. 2012. Noninvasive Monitoring of Soil Static Characteristics and Dynamic States: A Case Study Highlighting Vegetation Effects on Agricultural Land. Vadose Zone J. 11(3): 0. doi: 10.2136/vzj2011.0195.

Corwin, D.L., and S.M. Lesch. 2003. Application of Soil Electrical Conductivity to Precision Agriculture: Theory, Principles, and Guidelines. Agron. J. 95: 17.

Corwin, D.L., and S.M. Lesch. 2005. Apparent soil electrical conductivity measurements in agriculture. Comput. Electron. Agric. 46(1–3): 11–43. doi: 10.1016/j.compag.2004.10.005.

Farahani, H.J., G.W. Buchleiter, and M.K. Brodahl. 2005. Characterization of apparent soil electrical conductivity variability in irrigated sandy and non-saline fields in Colorado. Trans.-Am. Soc. Agric. Eng. 48(1): 155.

Garré, S., I. Coteur, C. Wongleecharoen, T. Kongkaew, J. Diels, et al. 2013. Noninvasive Monitoring of Soil Water Dynamics in Mixed Cropping Systems: A Case Study in Ratchaburi Province, Thailand. Vadose Zone J. 12(2): 0. doi: 10.2136/vzj2012.0129.

Garré, S., M. Javaux, J. Vanderborght, L. Pagès, and H. Vereecken. 2011. Three-Dimensional Electrical Resistivity Tomography to Monitor Root Zone Water Dynamics. Vadose Zone J. 10(1): 412. doi: 10.2136/vzj2010.0079.

von Hebel, C., M. Matveeva, E. Verweij, P. Rademske, M.S. Kaufmann, et al. 2018. Understanding Soil and Plant Interaction by Combining Ground-Based Quantitative Electromagnetic Induction and Airborne Hyperspectral Data. Geophys. Res. Lett. 45(15): 7571–7579. doi: 10.1029/2018GL078658.

von Hebel, C., S. Rudolph, A. Mester, J.A. Huisman, P. Kumbhar, et al. 2014. Three-dimensional imaging of subsurface structural patterns using quantitative large-scale multiconfiguration electromagnetic induction data. Water Resour. Res. 50(3): 2732–2748. doi: 10.1002/2013WR014864.

Huang, J., R. Purushothaman, A. McBratney, and H. Bramley. 2018. Soil Water Extraction Monitored Per Plot Across a Field Experiment Using Repeated Electromagnetic Induction Surveys. Soil Syst. 2(1): 11. doi: 10.3390/soilsystems2010011.

Jayawickreme, D.H., R.L. Van Dam, and D.W. Hyndman. 2010. Hydrological consequences of land-cover change: Quantifying the influence of plants on soil moisture with time-lapse electrical resistivity. GEOPHYSICS 75(4): WA43–WA50. doi: 10.1190/1.3464760.

King, J.A., P.M.R. Dampney, R.M. Lark, H.C. Wheeler, R.I. Bradley, et al. 2005. Mapping Potential Crop Management Zones within Fields: Use of Yield-map Series and Patterns of Soil Physical Properties Identified by Electromagnetic Induction Sensing. Precis. Agric. 6(2): 167–181. doi: 10.1007/s11119-005-1033-4.

Laloy, E., M. Javaux, M. Vanclooster, C. Roisin, and C.L. Bielders. 2011. Electrical Resistivity in a Loamy Soil: Identification of the Appropriate Pedo-Electrical Model. Vadose Zone J. 10(3): 1023. doi: 10.2136/vzj2010.0095.

Lavoué, F., J. Van Der Kruk, J. Rings, F. André, D. Moghadas, et al. 2010. Electromagnetic induction calibration using apparent electrical conductivity modelling based on electrical resistivity tomography. Surf. Geophys. 8(6): 553–561.

Ma, R., A. McBratney, B. Whelan, B. Minasny, and M. Short. 2011. Comparing temperature correction models for soil electrical conductivity measurement. Precis. Agric. 12(1): 55–66. doi: 10.1007/s11119-009-9156-7.

Martini, E., U. Werban, S. Zacharias, M. Pohle, P. Dietrich, et al. 2017. Repeated electromagnetic induction measurements for mapping soil moisture at the field scale: validation with data from a wireless soil moisture monitoring network. Hydrol. Earth Syst. Sci. 21(1): 495–513. doi: 10.5194/hess-21-495-2017.

McNeill, J.D. 1980. Electromagnetic terrain conductivity measurement at low induction numbers. Geonics Limited Ontario, Canada.

Michot, D., Y. Benderitter, A. Dorigny, B. Nicoullaud, D. King, et al. 2003. Spatial and temporal monitoring of soil water content with an irrigated corn crop cover using surface electrical resistivity tomography: SOIL WATER STUDY USING ELECTRICAL RESISTIVITY. Water Resour. Res. 39(5): n/a–n/a. doi: 10.1029/2002WR001581.

Moghadas, D., K.Z. Jadoon, and M.F. McCabe. 2017. Spatiotemporal monitoring of soil water content profiles in an irrigated field using probabilistic inversion of time-lapse EMI data. Adv. Water Resour. 110: 238–248. doi: 10.1016/j.advwatres.2017.10.019.

Rhoades, J.D., P.A.C. Raats, and R.J. Prather. 1976. Effects of liquid-phase electrical conductivity, water content, and surface conductivity on bulk soil electrical conductivity. Soil Sci. Soc. Am. J. 40(5): 651–655.

Robinson, D.A., H. Abdu, I. Lebron, and S.B. Jones. 2012. Imaging of hill-slope soil moisture wetting patterns in a semi-arid oak savanna catchment using time-lapse electromagnetic induction. J. Hydrol. 416–417: 39–49. doi: 10.1016/j.jhydrol.2011.11.034.

Shanahan, P.W., A. Binley, W.R. Whalley, and C.W. Watts. 2015. The Use of Electromagnetic Induction to Monitor Changes in Soil Moisture Profiles beneath Different Wheat Genotypes. Soil Sci. Soc. Am. J. 79(2): 459. doi: 10.2136/sssaj2014.09.0360.

Srayeddin, I., and C. Doussan. 2009. Estimation of the spatial variability of root water uptake of maize and sorghum at the field scale by electrical resistivity tomography. Plant Soil 319(1–2): 185–207. doi: 10.1007/s11104-008-9860-5.

Stanley, J.N., D.W. Lamb, G. Falzon, and D.A. Schneider. 2014. Apparent electrical conductivity (ECa) as a surrogate for neutron probe counts to measure soil moisture content in heavy clay soils (Vertosols). Soil Res. 52(4): 373. doi: 10.1071/SR13142.

Viscarra Rossel, R.A., V.I. Adamchuk, K.A. Sudduth, N.J. McKenzie, and C. Lobsey. 2011. Chapter Five - Proximal Soil Sensing: An Effective Approach for Soil Measurements in Space and Time. In: Sparks, D.L., editor, Advances in Agronomy. Academic Press. p. 243–291

Wasson, A.P., G.J. Rebetzke, J.A. Kirkegaard, J. Christopher, R.A. Richards, et al. 2014. Soil coring at multiple field environments can directly quantify variation in deep root traits to select wheat genotypes for breeding. 65(21): 6231–6249. doi: 10.1093/jxb/eru250.

Wasson, A.P., R.A. Richards, R. Chatrath, S.C. Misra, S.V.S. Prasad, et al. 2012. Traits and selection strategies to improve root systems and water uptake in water-limited wheat crops. J. Exp. Bot. 63(9): 3485–3498. doi: 10.1093/jxb/ers111.

Waxman, M.H., and L.J.M. Smits. 1968. Electrical conductivities in oil-bearing shaly sands. Soc. Pet. Eng. J. 8(02): 107–122.